Electronic Supplementary Material (ESI) for Nanoscale.

Supplementary Information for:

Layer-Dependent In-Plane Thermal Conductivity of Suspended MoS_2 Grown by Chemical Vapor Deposition

Jung Jun Bae, [a,b] Hye Yun Jeong, [a,b] Gang Hee Han, [a,b] Jaesu Kim, [a,b] Hyun Kim, [a,b] Min Su Kim, [a,b] Byoung Hee Moon, [a,b] Seong Chu Lim,[*,a,b] and Young Hee Lee[*,a,b,c]

[a]*Center for Integrated Nanostructure Physics, Institute for Basic Science (IBS), Sungkyunkwan University, Suwon 440-746, Republic of Korea*

[b]*Department of Energy Science, Sungkyunkwan University, Suwon 440-746, Republic of Korea*

[c]*Department of Physics, Sungkyunkwan University, Suwon 440-746, Republic of Korea*

Corresponding authors: (S. C. Lim) [*]seonglim@skku.edu and (Y. H. Lee) [*]leeyoung@skku.edu

Supplementary Information

S1. Raman measurement with a vacuum system

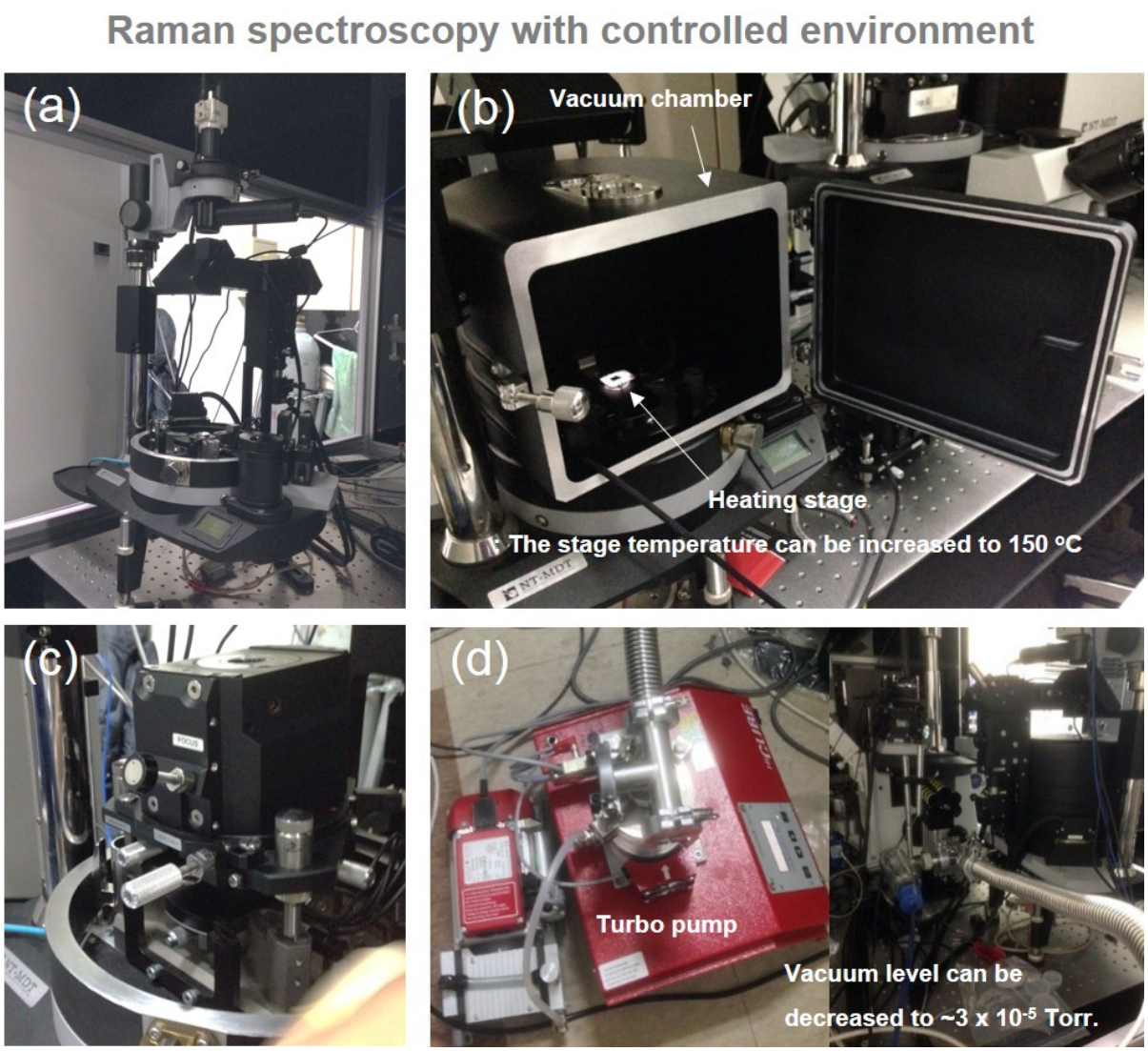

Figure S1. (a) The confocal Raman spectroscopy system. (b) The vacuum chamber and the heating stage. (c) The 100 × objective lens. (d) The turbo pump with the pressure gauge.

S2. CVD-grown monolayer, bilayer and multilayer MoS_2 on the SiO_2 substrate

Figure S2a shows the monolayer, bilayer and multilayer MoS_2 films that were transferred onto the SiO_2 substrate during one synthesis process. The number of layers in the MoS_2 films was confirmed by analyzing the peak separation of E^1_{2g} and A_{1g} peaks from the Raman spectra in Fig. S2b, and by analyzing the z-height profiles (Fig. S2e) of the topographic AFM images in Fig. S2c and S2d.

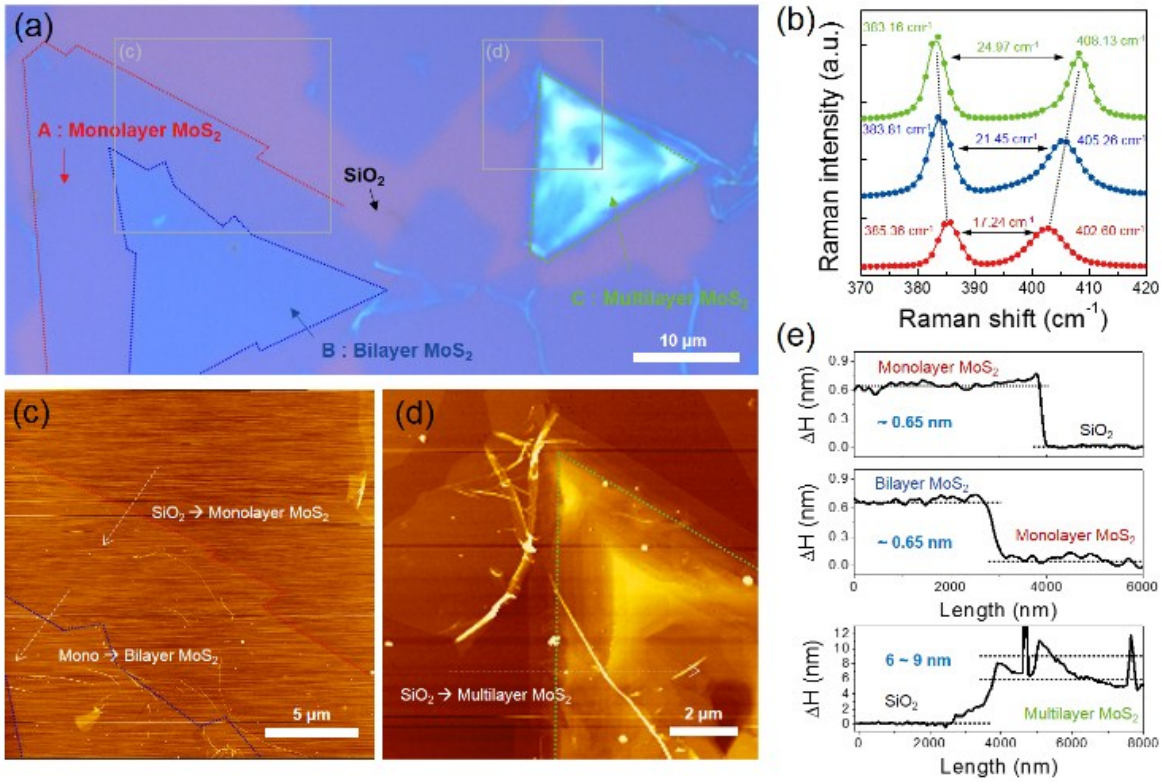

Figure S2. (a) The optic image of the MoS_2 films transferred onto the SiO_2/Si substrate. (b) The Raman spectra of the monolayer, bilayer, and multilayer MoS_2. The AFM images of the (c) monolayer and bilayer and (d) multilayer MoS_2 regions. (e) The z-height profiles of the monolayer, bilayer, and multilayer MoS_2. Black arrows indicate the MoS_2 wrinkles appeared during synthesis or transfer process in Fig. S2d and S2e.

S3. Temperature dependence of Raman spectroscopy

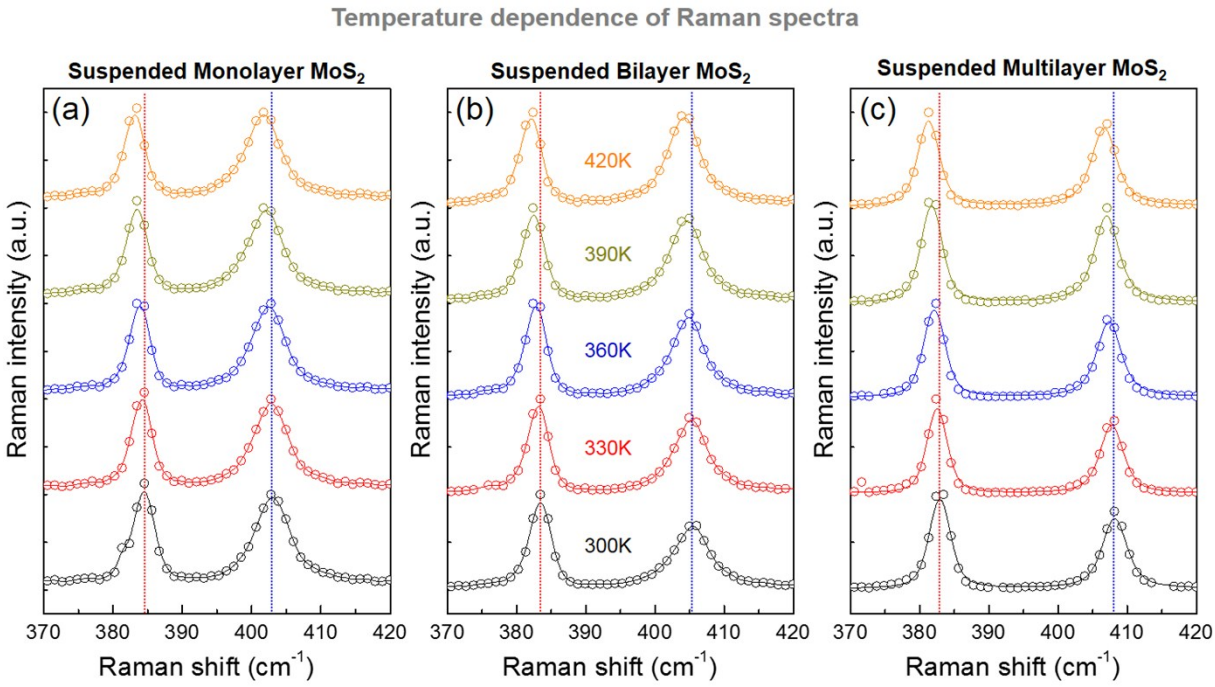

Figure S3. The Raman spectra for the (a) monolayer, (b) bilayer, and (c) multilayer MoS_2, at different temperatures.

S4. Laser power dependence of Raman spectroscopy

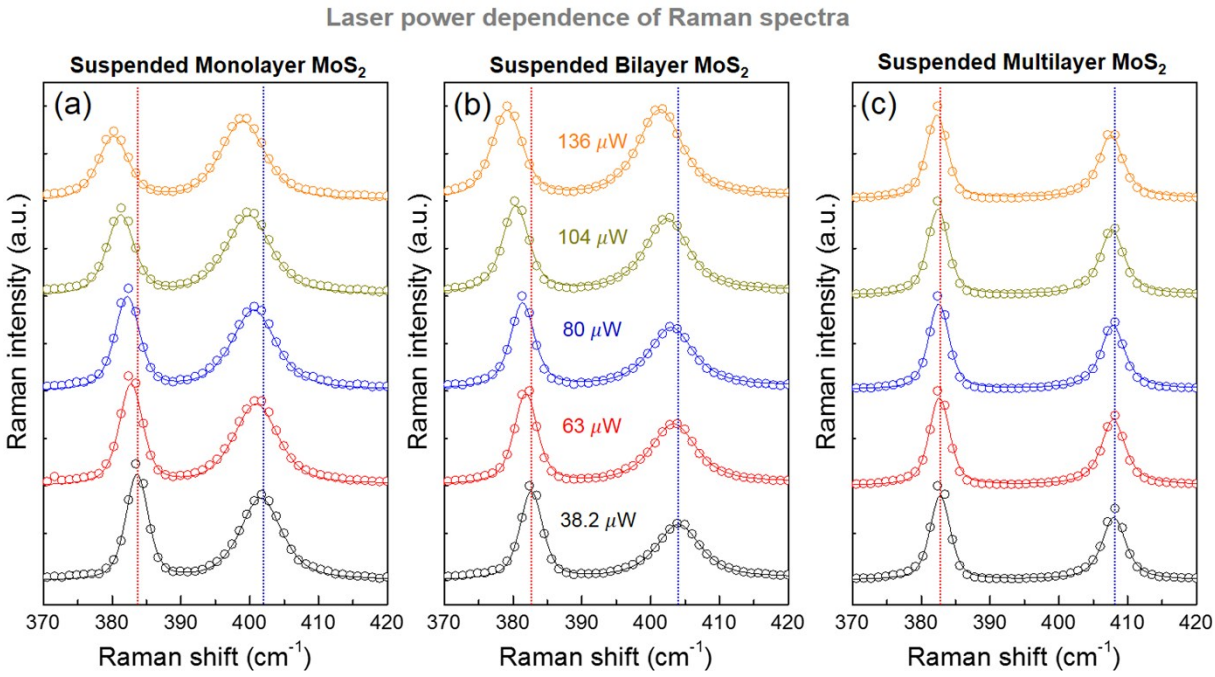

Figure S4. The Raman spectra for the (a) monolayer, (b) bilayer, and (c) multilayer MoS_2, for different laser power values.

S5. FEM simulations of the temperature profile

We used the finite elements method (FEM) with heat transfer module of the Comsol Multiphysics software package to investigate the temperature profiles in the suspended MoS_2 films. First, we designed the geometry as in Fig. S5(a), to obtain the temperature profiles in our structure of interest. The substrate was modeled as a combination of silicon, silicon dioxide and Au thin films with respective thicknesses of 500 μm, 300 nm, and 500 nm. Afterwards, we created cylindrical holes, 3.7 μm in diameter and 5 μm in depth. Finally, atop the Au layer we created a 0.65-nm-thick MoS_2 layer. The area for this geometry was 100 × 100 μm.

For this modeling, we extracted the material physical properties for Si, SiO_2 and Au from the material library of Comsol Multiphysics. For MoS_2, we took the value of thermal conductivity from Table 2.

To set up the physics, we used the "Heat Transfer in Solids" model and incorporated the heat source, expressed by the Gaussian function, into the governing heat transfer equation. Basically, the interface provides the equations, the boundary conditions, and the sources for modeling. We modeled the laser beam as a heat source by the Gaussian function:

$$\frac{P\alpha}{\left(\pi r_0^2\right)t} exp\left(-\frac{x^2+y^2}{r_0^2}\right) \qquad (11)$$

We assumed that the heat losses due to convection and radiation can be neglected and the temperature of the bottom face of the silicon domain was assumed to be ambient (300 K).

An additional computational optimization was focused on meshing. The generated fine meshes yielded highly accurate temperature profiles. The minimal and the maximal element sizes for both the MoS_2 films and the bottom layer were 0.005 and 0.006 μm, respectively. All simulations were performed in a 3D model.

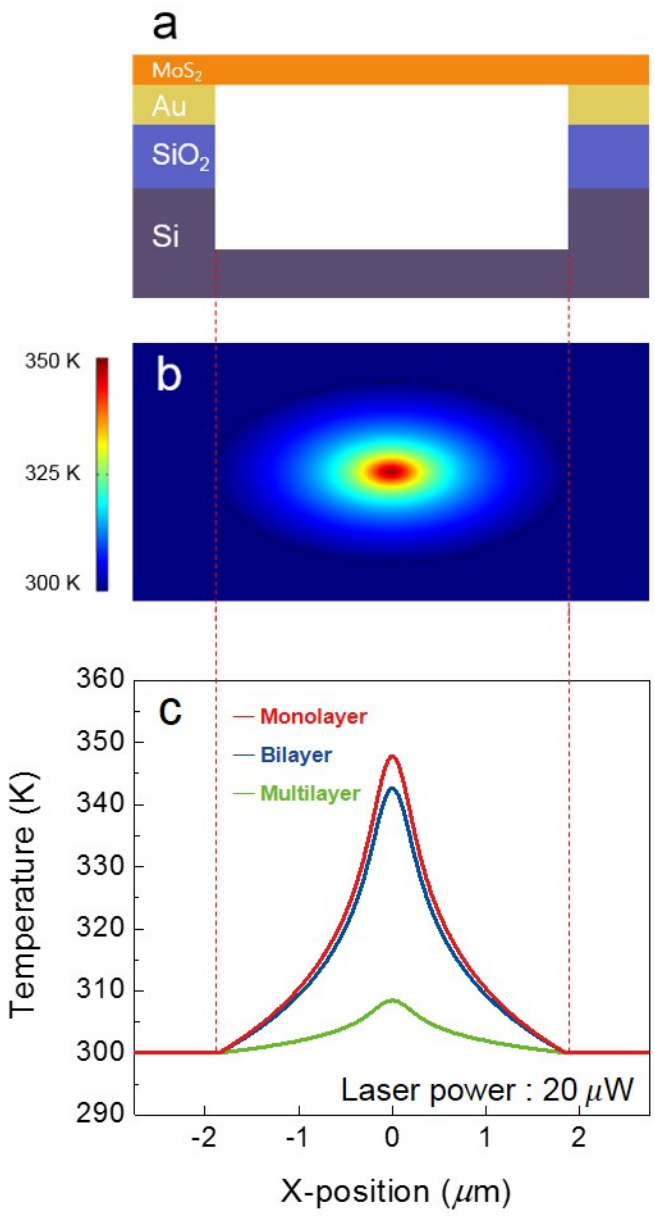

Figure S5. Schematics of (a) the suspended MoS_2 film on the 500-μm-thick silicon, 300-nm-thick silicon dioxide, and 500-nm-thick Au thin film with 3.7 μm diameter and 5 μm depth cylindrical hole-array. (b) Temperature distribution for the monolayer MoS_2 film on the Au substrate and (c) temperature profiles for the different MoS_2 films.

S6. Evaluation of thermal conductivity

To estimate the MoS_2 thermal conductivity by using Raman approach, the heat equation without convective heat loss was used for evaluating the temperature profile of the MoS_2 sample membranes inside a microcavity, with four boundary conditions: i) the temperature and ii) the temperature gradient at the cavity edge are continuous, iii) the temperature of a MoS_2 film on the Au substrate converges to the ambient temperature at a remote distance from the cavity center, and iv) the heat energy at the center of the suspended MoS_2 film is equal to the heat absorbed following the laser illumination in the steady state. Using these boundary conditions, the temperature distributions in the suspended and supported regions, $T_1(r)$ and $T_2(r)$, respectively, are

$$\kappa \frac{1}{r}\frac{d}{dr}\left[r\frac{dT_1(r)}{dr}\right] + q(r) = 0 \qquad \text{for} \quad r < R \qquad (1)$$

$$\kappa' \frac{1}{r}\frac{d}{dr}\left[r\frac{dT_2(r)}{dr}\right] - \frac{G}{t}\left[T_2(r) - T_a\right] = 0 \qquad \text{for} \quad r > R \qquad (2)$$

where κ and κ' are the thermal conductivity are the thermal conductivity of the suspended and supported MoS_2, respectively, r is the radial distance from the cavity center, R = 1.85 μm is the cavity radius, T_a is the ambient temperature, G is the interfacial thermal conductance between the MoS_2 sample and the Au substrate, and t is the MoS_2 film thickness. In the above equations, the heat generation term, $q(r)$, was described by volumetric Gaussian laser beam heating:

$$q(r) = \frac{I\alpha}{t} exp\left(-\frac{r^2}{r_0^2}\right) \qquad (3)$$

where α is the MoS_2 film absorbance at the wavelength of 473 nm, t is the MoS_2 film thickness, r_0 = 0.17 μm is the Gaussian laser beam radius. P is the incident laser power, measured by using a laser power-meter.

The general solutions to Eqs. (1) and (2) are:

$$T_1(r) = c_1 + c_2 \ln(r) + c_3 Ei\left(-\frac{r^2}{r_0^2}\right) \qquad \text{for} \quad r < R \qquad (4)$$

$$T_2(\gamma) = c_4 I_0(\gamma) + c_5 K_0(\gamma) + T_a \qquad \text{for} \quad r > R \qquad (5)$$

where where c_i are arbitrary constants, $Ei(x)$ is the exponential integral, $\gamma = r \cdot \left(\frac{G}{\kappa' t}\right)^{1/2}$, and the two homogeneous solutions $I_0(\gamma)$ and $K_0(\gamma)$ are the zeroth-order modified Bessel functions of the first and second kind, respectively.

The boundary conditions that yield the values of constants c_i are:

$$T_1(R) = T_2(\gamma)\big|_{r=R} \tag{6}$$

$$T_2(r \to \infty) = T_a \tag{7}$$

$$-\kappa \frac{dT_1(r)}{dr}\bigg|_{r=R} = -\kappa' \frac{dT_2(\gamma)}{dr}\bigg|_{r=R} \tag{8}$$

$$-2\pi R t \kappa' \frac{dT_2(\gamma)}{dr}\bigg|_{r=R} = \alpha P \tag{9}$$

We used Mathematica (Wolfram Research) to determine the values of constants c_i by using these boundary conditions and Equation (4) and (5). From this calculation, we obtained the temperature profile in the suspended MoS_2 film, $T_1(r)$. Finally, the weighted average temperature in the beam spot, T_m, measured by using Raman spectroscopy, can be approximated by using the obtained $T_1(r)$ and $q(r)$:

$$T_m \approx \frac{\int_0^{r_0} T_1(r) q(r) r dr}{\int_0^{r_0} q(r) r dr} \tag{10}$$

The expression for T_m involves several parameters: the measured laser power P, the MoS_2 absorbance α, and the MoS_2 thermal conductivities κ and κ'. Here, we assumed that the thermal conductivities of the suspended and supported MoS_2 samples are the same ($\kappa = \kappa'$), and we assumed G = 50 MW m^{-2} K^{-1}. We used the numerical values of T_a= 300 K, t = 0.65 nm, α = 0.045 for the monolayer MoS_2 to obtain the thermal conductivity of 13.3 ± 0.3 W m^{-1} K^{-1}. The thermal conductivities of MoS_2 films with different thicknesses can be obtained by using the same methods.

S7. Absorbance of MoS_2 films vs. the number of layers

For the absorption spectral mappings, we prepared the MoS_2 films that were transferred onto the quartz substrate (Fig. S7(a)) and we measured the film thicknesses to confirm the number of layers by using AFM (Fig. S7(b)). First, background transmission spectrum were obtained from transparent area near the samples on the quartz substrate. Then, we divided all of the transmission spectra by the corresponding background transmission spectrum to obtain absorption spectral mapping. The absorption intensity mapping for the MoS_2 films with different thicknesses is shown in Fig. S7(c). In Fig. S7(d), the absorption intensity increases with the sample thickness. For the conductivity calculation, we chose the absorbance values at the wavelength of 473 nm.

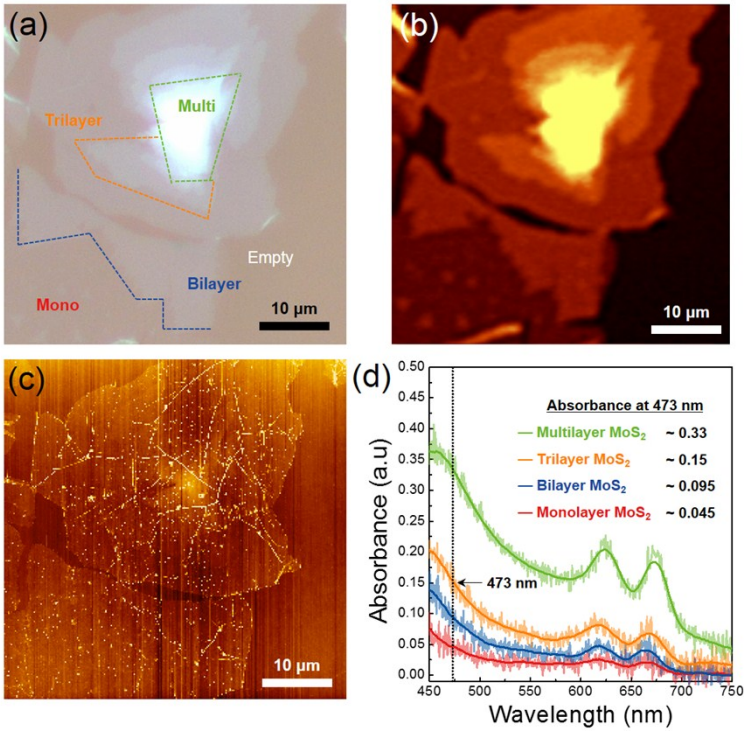

Figure S7. (a) Optical image, (b) AFM image, (c) absorbance spectral mapping image and (d) absorbance spectra for the supported MoS_2 films (on the quartz substrate) with different thicknesses.

S8. Effects of absorbance and environment

We used the Mathematica software to investigate the effects of absorbance on the thermal conductivity of the suspended MoS_2 films (Fig. S8a). To determine the effect of measurement environment, Raman spectra were obtained under vacuum and ambient conditions. The different slope of ΔT vs. ΔP, shown in Fig. S8b, could be obtained due to convective heat loss[1] and de-doping process.[2]

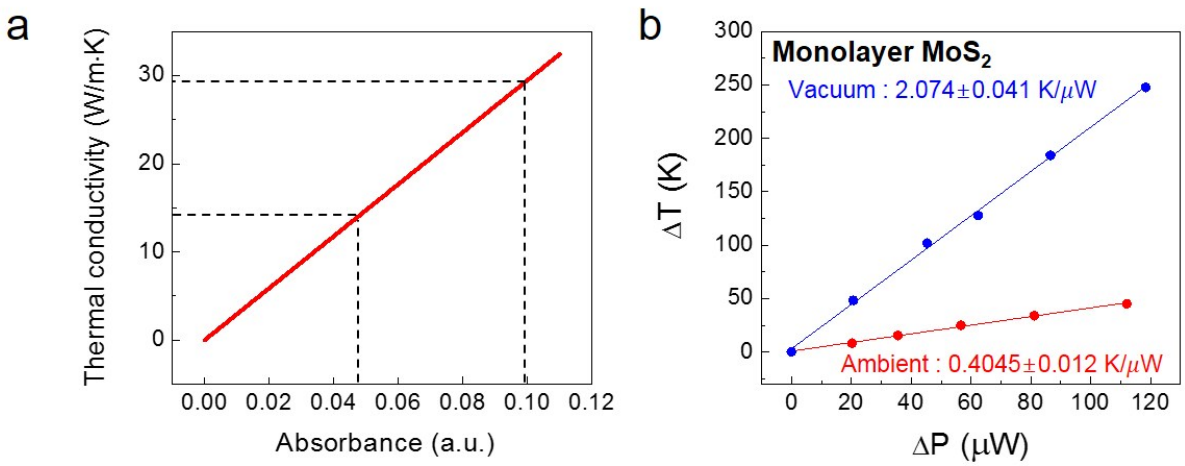

Figure S8. (a) The calculated thermal conductivity vs. the absorbance. (b) The obtained ΔT vs. ΔP under vacuum and ambient conditions.

S9. Electronic thermal conductivity

In solids, the heat transport is mediated by both electrons and phonons. The heat conduction by electrons, κ_e, can be estimated from the Wiedemann-Franz law, $\frac{\kappa_e}{\sigma} = LT$,[3] where L is the Lorentz number and σ is the electrical conductivity. L can be further defined by $L = \frac{\pi^2 k_B^2}{3e}$, where k_B is the Boltzmann constant and e is the elementary charge. The electrical conductivity of suspended MoS_2 films is ~75 S m^{-1} and ~107 S m^{-1} for 1-nm-thick and 7-nm-thick layers, respectively.[4] Using the Lorentz number of 1.5 × 10^{-8} WΩ K^{-2} for non-degenerate semiconductors,[5] the electronic thermal conductivity values of the studied MoS_2 films range from ~3.4 × 10^{-4} W m^{-1} K^{-1} for the monolayer to ~4.8 × 10^{-4} W m^{-1} K^{-1} for the multilayer (Fig. S9). Although the electronic thermal conductivity of MoS_2, κ_e, increases owing to the increasing electrical conductivity with the increasing number of layers, the contribution of electronic thermal conductivity to the total thermal conductivity is weaker by ~10^5 than the measured thermal conductivity of MoS_2.

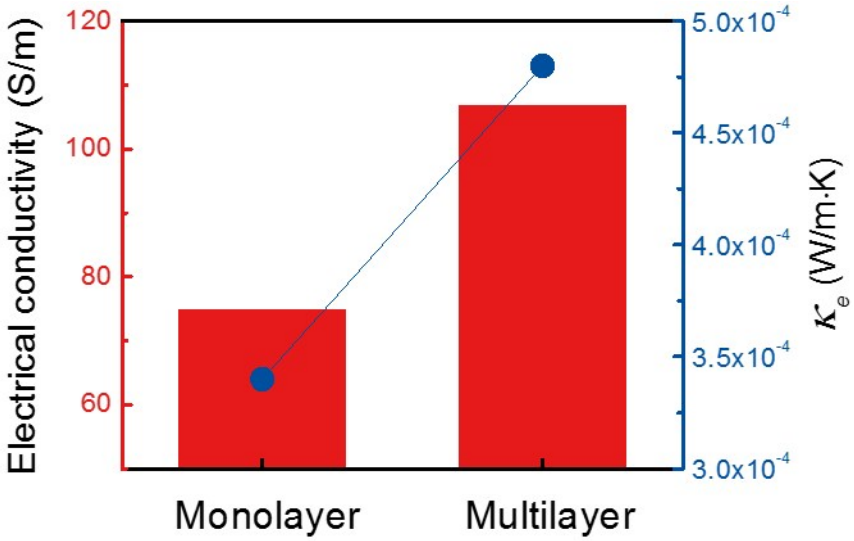

Figure S9. Electrical conductivity of the suspended monolayer and multilayer MoS_2 (red bar and left axis) and the calculated electronic thermal conductivities, κ_e, from Wiedemann-Franz law (blue circle and right axis).

S10. Phononic thermal conductivity

The phononic thermal conductivity can be expressed by the Boltzmann transport equation (BTE) as $\kappa_{ph} = \sum_i \int C_{ph,i}(\omega) v_i(\omega) l_i(\omega) d\omega$,[6] where $C_{ph,i}(\omega)$ is the volumetric specific heat capacity, $v_i(\omega)$ is the group velocity, and $l_i(\omega)$ is the mean free path (MFP) for a phonon in the i^{th} phonon branch. The thermal conductivity is dominated by three acoustic phonon modes (i = LA, TA, ZA) owing to their larger group velocities compared with optical phonon modes. The contributions of different physical parameters to the phononic thermal conductivity of MoS_2 are reviewed in the following paragraphs.

S10-1. Specific heat capacity of MoS_2

The volumetric specific heat capacity of each phonon branch is given as $C_{ph,i}(\omega) = \int_0^{\omega_D} k_B \left(\frac{\hbar\omega}{k_B T}\right)^2 \frac{e^{\hbar\omega/k_B T}}{\left(e^{\hbar\omega/k_B T} - 1\right)^2} g(\omega) d\omega$,[6] where $\hbar$ is the reduced Planck constant, ω is the phonon angular frequency, $g(\omega)$ is the phonon density of states (DOSs), and ω_D is the material's Debye frequency. Therefore, the specific heat capacity is directly related to $g(\omega)$ that depends on the dimensionality. As the number of layers increases, the acoustic phonon DOSs increases. This is due to an increase in the number of degrees of freedom associated with lattice vibrations with increasing number of dimensions. Therefore, the specific heat capacity C below the Debye temperature (which is ~600 K for MoS_2)[7] is $C \sim T^d$, where d is the dimensionality. Within the Debye approximation, $\omega = v \cdot k$, where v is the sound

velocity and k is the wave vector. Consequently, the specific heat capacity of MoS_2 near room temperature should increase with the increasing number of layers. For instance, both the experimental and the theoretical results show that the monolayer specific heat capacity is higher than that of bulk MoS_2 at room temperature.[8,9]

S10-2. Group velocity of acoustic phonon modes

When acoustic phonons below 200 cm^{-1} are considered, the group velocities of the three acoustic phonon branches of the monolayer MoS_2 are estimated to be 5.68 × 10^3 m s^{-1}, 4.39 × 10^3 m s^{-1}, and 3.75 × 10^3 m s^{-1} for the LA, TA, and ZA modes, respectively.[8,10,11] The *ab initio* calculation of the phonon dispersion relation suggests that the group velocity of the ZA phonon for the monolayer MoS_2 is comparable or slightly lower than that of the LA and TA modes inside a Brillouin zone. In contrast to the monolayer MoS_2, while the group velocities of the LA and TA modes are not significantly changed, the group velocity of the ZA phonon drops to nearly zero at the zone center in a bulk.[12]

S10-3. Mean free path of acoustic phonon modes

The phonon MFP is related to the group velocity and relaxation time through the expression, $l_i(\omega) = v_i(\omega)\tau_i(\omega)$, where τ_i is the phonon relaxation time.[6] In the relaxation time approximation (RTA), various scattering mechanisms limiting the MFP are usually related through $\tau_i^{-1} = \Sigma_j \tau_{j,i}^{-1}$ (j denotes different scattering mechanisms related to defects, electrons, phonons, and the surface).[6] By considering phonon-phonon scattering due to the crystal lattice anharmonicity and phonon-boundary scattering due to the surface boundary, the overall phonon relaxation rate τ_i^{-1} is the sum of the contributions from phonon scattering ($\tau_{p,i}^{-1}$) and boundary scattering ($\tau_{b,i}^{-1}$):[6]

$$\frac{1}{\tau_i} = \frac{1}{\tau_{p,i}} + \frac{1}{\tau_{b,i}} \qquad (11)$$

An analytical expression for the relaxation time due to the dominant anharmonic three-phonon mechanism can be written as:[10]

$$\frac{1}{\tau_{p,i}} = 2\gamma_{q,i}^{2}\frac{k_B T \omega^2}{M v^2 \omega_D} \quad (12)$$

In the above equation, M is the atomic mass, v is the group velocity, ω_D is the Debye frequency, and $\gamma_{q,i}$ is the Grüneisen parameter of each phonon mode at the point q, given by:[10]

$$\gamma_{q,i} = -\frac{a}{2\omega_i(q)}\frac{d\omega_i(q)}{da} \quad (13)$$

In the case of the monolayer MoS_2, the Grüneisen parameters, measuring anharmonic crystal vibrations at the Γ point for the different acoustic phonon modes (ZA, TA, and LA) are 159.7, 58.6, and 25.3, respectively.[10] In particular, the ZA mode exhibits a large Grüneisen parameter.[10] Therefore, among the three acoustic phonon modes, the ZA mode scatters more than the other two phonon modes. For this reason, although the three acoustic phonon modes have similar group velocities, the phonon MFP for the ZA phonon mode is under 1 nm, whereas those for the LA and TA modes are 18.1 nm and 5.0 nm, respectively.[10] The total phonon MFP for MoS_2 is ~20 nm, which is almost two orders of magnitude smaller than that for suspended graphene. In the monolayer MoS_2, owing to a larger group velocity and a longer relaxation time of the LA phonon mode, the MFP for the LA phonon mode is larger than that for the ZA phonon mode, over the whole range of acoustic phonon frequencies, up to 240 cm^{-1}. Therefore, the contribution of the LA mode to the thermal conductivity of monolayer MoS_2 is more significant than that of the ZA mode.[10,13]

From the viewpoint of specific heat capacity, the increase in specific heat capacity is not sufficient for explaining the increase in thermal conductivity observed in our study. In addition, as the number of layers increases, the group velocity of the major heat transporter (the LA phonon) is not significantly affected. In addition, because the dependence of phonon-phonon scattering on the interlayer interaction does not change, we do not expect to observe significant reduction in MoS_2 thermal conductivity with increasing number of layers.

S10-4. Layer-dependent thermal conductivity of graphene

The thermal property of MoS_2 is qualitatively different from that of graphene. In the case of monolayer graphene, ZA phonons carry more heat energy than LA and TA phonons.[14] The group velocity of the ZA phonon is comparable to the LA phonon at the zone boundary[15,16] and the DOSs of the ZA phonon is much larger than both of the LA and TA phonon modes.[14] Furthermore, owing to the selection rule for ZA-related phonon-phonon scattering, the scattering of the ZA mode is suppressed, stemming from the low Grüneisen parameter.[17] However, the selection rule is invalidated as the graphene starts interacting with a substrate and neighboring layers, which causes an increase in the lattice inharmonicity. Hence, the thermal conductivity of monolayer graphene, dominated by the ZA phonon mode, sharply decreases as the number of layers increases.

S10-5. Intrinsic phonon mean free path of monolayer and bulk MoS_2

Intrinsic phonon MFP depends on the group velocity v_i from phonon dispersion and the phonon relaxation rate τ_i^{-1} which is related to scattering process. As the number of layers increases, the group velocity of phonons is not significantly affected as described in S10-3. Among the several scattering process, the boundary scattering at the surface is a result of surface phenomenon, not an intrinsic scattering process. Therefore, thickness-dependent intrinsic phonon MFP of MoS_2 is affected by only phonon-phonon scattering.

Recently, the ZA mode has been shown to significantly contribute to the thermal conductivity of layered materials, such as graphene and h-BN.[14,18,19] In the case of graphene, the symmetry selection rule plays a key role in the ZA phonon-phonon scattering.[18] Interaction between graphene layers in multilayer graphene (MLG) and graphite breaks the a selection rule on phonon-phonon scattering and causes the phase space for the three-phonon scattering to become very large and increase rapidly with the number of layers.[14] Unlike graphene, monolayer MoS_2 is a non-centrosymmetric material;[20,21] thus, the selection rule theory of phonon-phonon scattering cannot be adapted for MoS_2.

Moreover, MoS_2 has a phononic bandgap between the acoustic and optical phonon branches.[22] As a result, the number of the phonon-phonon scattering channels between the acoustic and optical branches

hardly changes with the increasing number of MoS_2 layers. This behavior is contrasted to that of graphene, in which the number of the phonon-phonon scattering channels increases due to the crossover of the acoustic and optical phonon branches in the phonon dispersion.[22,23] Hence, a change in the phonon-phonon scattering for few-layer and bulk MoS_2 could be minute. As a result, because the group velocity and the phonon-phonon scattering, which is hardly changed, we do not expect a significant change in intrinsic phonon MFP with the increasing number of layers in MoS_2. It is thus expected that similar value in the phonon MFP of monolayer and bulk MoS_2. Recently, it has been reported that monolayer MoS_2 exhibited a calculated phonon MFP of 5.2 nm (molecular dynamics simulations),[24] 14.6 nm (first-principles calculations),[13] and ~ 20 nm (density functional perturbation theory)[10] at room temperature. Our predicted value of phonon MFP of bulk MoS_2, 5~20 nm is similar to the our best-fit values of $\Lambda_{bulk} =$ 17 nm in Fig. 7.

References

1. S. Chen, A. L. Moore, W. Cai, J. W. Suk, J. An, C. M. C. Amos, C. W. Magnuson, J. Kang, L. Shi, R. S. Ruoff, *ACS Nano,* 2011, **5,** 321.
2. H. Nan, Z. Wang, W. Wang, Z. Liang, Y. Lu, Q. Chen, D. He, P. Tan, F. Miao, X. Wang, J. Wang, Z. Ni, *ACS Nano* 2014, **8,** 5738.
3. R. Franz, and G. Wiedemann, Ann. Phys., 1853, **165,** 497.
4. F. Wang, P. Stepanov, M. Gray, and C. N. Lau, Nanotechnology, 2015, **26,** 105709.
5. H. S. Kim, Z. M. Gibbs, Y. Tang, H. Wang, and G. J. Snyder, APL Mater., 2015, **3,** 041506.
6. D. L. Nika, and A. A. Balandin, J. Phys.: Condens. Matter, 2012, **24,** 233203.
7. N. Wakabayashi, H. G. Smith, and R. M. Nicklow, Phys. Rev. B, 1975, **12,** 659.
8. J. Su, Z. T. Liu, L. P. Feng, and N. Li, J. Alloy Compd., 2015, **622,** 777.
9. C. Ataca, M. Topsakal, E. Aktürk, and S. A. Ciraci, J. Phys. Chem. C, 2011, **115,** 16354.
10. Y. Q. Cai, J. H. Lan, G. Zhang, and Y. W. Zhang, Phys. Rev. B, 2014, **89,** 035438.

11. X. Li, J. T. Mullen, Z. Jin, K. M. Borysenko, M. B. Nardelli, and K. W. Kim, Phys. Rev. B, 2013, **87,** 115418.

12. A. Molina-Sanchez, L. Wirtz, Phys. Rev. B 2011, **84,** 155413.

13. X. L. Wei, Y. C. Wang, Y. L. Shen, G. F. Xie, H. P. Xiao, J. X. Zhong, and G. Zhang, Appl. Phys. Lett., 2014, **105,** 103902.

14. L. Lindsay, D. A. Broido, and N. Mingo, Phys. Rev. B, 2010, **82,** 115427.

15. S. Ghosh, W. Z. Bao, D. L. Nika, S. Subrina, E. P. Pokatilov, C. N. Lau, and A. A. Balandin, Nat. Mater., 2010, **9,** 555.

16. D. L. Nika, E. P. Pokatilov, A. S. Askerov, and A. A. Balandin, Phys. Rev. B, 2009, **79,** 155413.

17. D. K. C. Macdonald, and S. K. Roy, Phys. Rev., 1955, **97,** 673.

18. M. M. Sadeghi, I. Jo, L. Shi, *PNAS,* 2013, **110,** 16321.

19. L. Lindsay, D. A. Broido, *Phys. Rev. B,* 2011, **84,** 155421.

20. S. Wu, J. S. Ross, G. B. Liu, G. Aivazian, A. Jones, Z. Fei, W. Zhu, D. Xiao, W. Yao, D. Cobden, X. Xu, *Nat. Phys.,* 2013, **9,** 149.

21. R. Suzuki, M. Sakano, Y. J. Zhang, R. Akashi, D. Morikawa, A. Harasawa, K. Yaji, K. Kuroda, K. Miyamoto, T. Okuda, K. Ishizaka1, R. Arita, Y. Iwasa, *Nat. Nanotech.,* 2014, **9,** 611.

22. Z. W. Ding, J. W. Jiang, Q. X. Pei, Y. W. Zhang, *Nanotechnology,* 2015, **26,** 065703.

23. J. W. Jing, H. S. Park, T. Rabczuk, *Nanoscale,* 2014, **6,** 3618.

24. X. Liu, G. Zhang, Q. Pei, Y. Zhang, *Appl. Phys. Lett.,* 2013, **103,** 133113.